International Journal of Technology 16(4) 1389-1407 (2025)

International Journal of Technology

http://ijtech.eng.ui.ac.id

Research Article

A Novel Approach to the Development of $Cu/ZnO/SiO_2$ Catalyst for the Hydrogenation of CO_2 into Methanol Using Induction Flow Levitation

Artyom N. Markov [1,*], Anna A. Golovacheva [1], Alexander A. Kapinos [1,2], Egor S. Dokin [1], Pavel P. Grachev [1], Anton N. Petukhov [1], Artem Atlaskin [2], Vitaly A. Medov [1], Sergey S. Suvorov [1], Andrey V. Vorotyntsev [1]

[1]Chemical Engineering Laboratory, Research Institute for Chemistry, Lobachevsky State University of Nizhny Novgorod, 603950 Nizhny Novgorod, Russia
[2] Laboratory of Smart Materials and Technologies, Mendeleev University of Chemical Technology of Russia, 125047 Moscow, Russia
[*]Corresponding author: markov.art.nik@gmail.com; Tel.: +78314623147

Abstract: This study aimed to explore the feasibility of using induction flow levitation method for synthesizing catalyst to facilitate methanol production. Two distinct types of catalyst were prepared on a silicon dioxide substrate through mechanochemical synthesis using copper and zinc oxide nanopowders (Cu/SiO_2 and $Cu/ZnO/SiO_2$). Subsequently, comprehensive characterization of the resulting nanoparticles and catalytic systems was conducted using a suite of physicochemical techniques. The investigation of catalytic activity was carried out within a continuous-flow reactor, in which methanol was obtained as the predominant reaction product. The results showed that during the experiment, a reduction in operating pressure was achieved with elevated methanol productivity and a significant carbon dioxide conversion rate. The catalyst containing ZnO nanoparticles demonstrated superior performance, achieving a maximum CO_2 conversion of 30.1% at 5 MPa and 300°C. The highest methanol yield, reaching 108 $mg/g_{cat}{\cdot}h$, was achieved at 280°C and 5 MPa. Throughout the experiments, carbon monoxide, methanol, ethanol, methyl formate, dimethyl ether, propanol, isobutyl, and isopropanol were detected.

Keywords: CO_2 hydrogenation; Heterogeneous catalysis; Induction flow levitation; Methanol; Nanoparticles

1. Introduction

Catalysis and associated derivatives processes are gaining increased significance within the chemical industry, serving as crucial technologies to ensure the sustainable advancement of manufacturing procedures. Numerous sectors, including chemical, petroleum, agricultural, high-molecular compound production, electronics, and pharmaceuticals, significantly depend on catalysis. Over 90% of chemical substances are, to a great extent, the outcome of catalytic processes, emphasizing the critical role of catalysis (Whulanza et al., 2024). Creating an effective catalytic process suitable for large-scale industrial applications is a challenging endeavor that requires significant resource investment (Busacca et al., 2011).

Typically, various types of raw materials are used for catalyst fabrication, including salts of catalytically active metals, sols, oxides, and natural minerals. The selection of a specific type of raw

---

This work was supported by the 'Russian Science Foundation' funded by 'Physical and chemical bases of direct controlled synthesis of nanoparticles, nanoclusters and volatile hydrides by the induction flow levitation method' No. 20-79-10097

https://doi.org/10.14716/ijtech.v16i4.7435
Received November 2024; Revised January 2025; Accepted March 2025

material depends on the catalyst composition, impurity content, and cost considerations. Raw materials must adhere to specific criteria including stability of chemical and phase composition, as well as absence of harmful additives, dispersity, and water content (Mulyatun et al., 2022). Furthermore, the homogeneity of the catalyst composition is primarily influenced by a multitude of factors including the consistency of the chemical composition of the raw material, particle size, moisture content, method and duration of production, as well as regulations on transportation, loading, and storage (Ren et al., 2022).

Considering all the factors listed above, which significantly influence the development of methodologies and technologies essential for catalyst synthesis, there is a complex task of managing the production of catalyst. This process must be capable of supplying consumers with the required quantity of catalyst within optimal timeframes while upholding the quality of the delivered products. However, in practice, the organization of industrial catalyst production is faced with several challenges (Madani et al., 2024). One of the significant challenges is the intricate coordination required for scaling up the production of different catalyst needed for diverse applications in the chemical industry. Additionally, significant energy and resource expenses are required to achieve the desired purity level of the product (Zhao et al., 2021).

CO_2 can be considered the most environmentally friendly source of carbon used to produce fuels and chemicals. The amount used for fuel production ranges from 1 to 4.2 gigatons per year (Hepburn et al., 2019). Therefore, the use of CO_2 can contribute to achieving global emission targets while meeting the increasing demand for fossil fuels and chemicals.

The main challenge in the conversion of CO_2 to methanol lies in the equilibrium limitations. The high stability of CO_2 and the poor reaction kinetics make it difficult to achieve high conversion rates at low temperatures. Additionally, during the conversion, methanol selectivity can be a challenge due to side reactions, such as the reverse conversion of water gas, which uses valuable hydrogen and generates CO and H_2O, decreasing the stability of the catalyst (Li et al., 2018; Bian et al., 2017; Zhao et al., 2017; Wang et al., 2011). The Fischer-Tropsch synthesis of hydrocarbons from CO_2 also suffers from very low product yields, as hydrocarbons are formed alongside oxygenates, depending on the catalyst, with a statistical distribution. These factors make the separation of the product a significant concern. Consequently, studies on thermocatalytic CO_2 hydrogenation are focused on finding catalyst that improve CO_2 activation and selectivity for desirable products, while inhibiting competing reaction pathways.

There is a pressing need to find improved catalyst for CO_2 conversion in all aspects. The diversity of these requirements has led to extensive studies on catalyst with more complex structures than traditional types. In general, traditional solid catalyst used in industrial processes consist of an active phase dispersed on a stable, porous support with a large specific surface area. Methods for preparing catalytic phases on supports, such as impregnation, precipitation, and sol-gel synthesis, are cost-effective on an industrial scale but lack precise control over the structure of the catalyst at the atomic level. Therefore, heterogeneous catalyst structures often exist, sometimes with poor dispersions of the active phase, compromising selectivity, activity, and stability.

Zinc-chromium and copper-containing catalyst are used to produce methanol from CO_2 (Meng et al., 2015). The synthesis of catalyst primarily occurs through two methods namely dry and wet. In the "dry" synthesis method, precise proportions of finely ground zinc oxide and chromium anhydride are initially blended in a dry state, with distilled water being subsequently added (Thao et al., 2017). The activity of the catalyst prepared through the "wet" method surpasses that of the "dry" method by 10-15% (Wahyono et al., 2022). Zinc-chromium catalyst is also obtained through coprecipitation from zinc and chromium nitrate salts. Upon the interaction with ammonium carbonate in solution, basic carbonate salts precipitate. During the calcination of the precipitate in a hydrogen atmosphere, zinc and chromium oxides react to form zinc chromite. The resulting catalyst mass is mixed with graphite after grinding and formed into tablets. The prepared catalyst shows a highly developed internal surface area (over 100 m^2) (Yin et al., 2021), a lower bulk density by 30-36%, and higher activity compared to the product obtained using the "dry" method.

Both the dry and wet methods have significant limitations, such as the risk of catalyst contamination with impurities (Ren et al., 2023), leading to decreased efficiency and increased emissions of harmful substances. This situation often requires the catalyst to be restored to the active state. The lack of one-step processes (Guo et al., 2021) in industrial catalyst synthesis for methanol production adds to the reduced energy efficiency of these methods, leading to higher final costs for consumers. Therefore, the task of developing a new synthesis approach for catalyst remains pertinent. The new approach must meet requirements such as single-step processing, high selectivity, and product yield, while also being less demanding in terms of resources and energy.

One of the promising types of catalytic systems used in practice is nano-sized catalyst (Kalubowila et al., 2021). These are a unique class of catalyst characterized by extremely small particle sizes, typically ranging from a few units to several tens of nanometers (Kusrini et al., 2024; Tuktin et al., 2024). Nano-sized catalyst possesses several outstanding properties and advantages, leading to the application in various chemical processes (Ying et al., 2021; Xie et al., 2020).

Nano-sized catalyst possess significantly larger active surface areas compared to macroscopic counterparts, as well as unique kinetics of the conducted reactions. This enables increased reaction rates and improved conversion of reactants. Catalyst can be intentionally crafted with a precisely regulated surface morphology (Gómez-Rodríguez et al., 2019), resulting in elevated selectivity towards particular reaction products and mitigating the formation of undesired by-products. Furthermore, nano-sized catalyst has enhanced thermal and chemical stability, which enables sustained activity at elevated temperatures (Pajor-Świerzy et al., 2022) or under aggressive chemical conditions (Khatami et al., 2018). Moreover, the catalyst possesses improved regeneration capabilities and can be readily restored after usage, ensuring stability and prolonged service life.

Currently, there are several conventional methods for obtaining nanoparticles, including chemical vapor deposition, the sol-gel method (Wang et al., 2022), laser ablation, thermal spraying, processes in microemulsions, planetary milling, plasma chemistry, deposition from ethereal solutions, deposition from high-temperature melts of salts, and cryochemistry (Karunakaran et al., 2023). Some of these methods, such as chemical vapor deposition and laser ablation, require high vacuum and multi-step processes, which are environmentally unfriendly and expensive due to equipment complexity (Khan et al., 2019).

The induction flow levitation (IFL) method opens up new prospects for obtaining nanoparticles. It offers high productivity (up to 200 g/h), controlled particle sizes across a wide range (0.5 – 500 nm), and non-contact heating (up to 2500 °C), ensuring product purity and adherence to the principles of "Green Chemistry"(Kusrini et al., 2015). This method is carried out by vaporizing metal in a suspended state using non-contact heating, allowing for the creation of metal nanoparticles and semiconductors with different sizes (Vorotyntsev et al., 2022; Markov et al., 2022). IFL is highly suitable for fabricating catalyst through mechanochemical synthesis.

Based on the discussion above, this study aimed to use a novel method for obtaining nanoparticles, namely induction flow levitation (IFL), followed by the preparation of catalyst for the process of CO_2 hydrogenation to facilitate methanol production. Traditionally, copper-based catalyst have been used in methanol production. However, recent studies have focused on the use of catalyst that include zinc oxide (Beck et al., 2024). The effectiveness of zinc oxide-based catalyst was reportedly confirmed using methods such as CO_2 and H_2 chemisorption. To increase the surface area of the catalyst, mesoporous SiO_2 was used as a support material.

$Cu/ZnO/SiO_2$ and Cu/SiO_2 catalytic systems were used and for this purpose, powders of copper and zinc oxide nanoparticles were synthesized by IFL. A highly porous silicon dioxide substrate was obtained by the sol-gel method using silicon tetrachloride, a by-product of the silicon industry, as a precursor to SiO_2 and polyethylene glycol (structurizer). For the first time, $Cu/ZnO/SiO_2$ and Cu/SiO_2 catalytic systems were obtained, preferably using a mechanochemical approach, namely by granulation in a tablet press. The physicochemical characterization of the obtained nanoparticles, SiO_2 substrates, and synthesized catalyst was carried out using methods such as transmission electron microscopy (TEM), high-resolution TEM (HREM), TEM with energy-dispersive X-ray spectroscopy (TEM-EDS), scanning electron microscopy (SEM) in combination with energy-dispersive X-ray spectroscopy (SEM-EDS), low-temperature porometry, X-ray diffraction (XRD), and inductively coupled plasma mass spectrometry (ICP-MS). Moreover, chemisorption experiments were conducted to determine the recovery temperature of the catalyst and the adsorption capacity of CO_2 and H_2. Catalytic tests of synthesized systems for the CO_2 hydrogenation reaction showed the best efficiency for catalyst with the addition of ZnO nanoparticles.

2. Experimental part

2.1. Materials

Copper wire of 0.2 mm diameter (99.9%) and zinc wire of 0.5 mm diameter (99.99%) were used as initial materials (Alfa Aesar, Germany). Dry isopropyl alcohol (Component-reactive Ltd., Russia), oxygen (99.999%), and argon (99.9995%) were sourced from Monitoring Ltd. (Russia). Polyethylene glycol (PEG) with a molecular weight of 1500 was obtained from Sigma-Aldrich (Germany). In addition, KCl, HCl, hexane, benzene, and toluene were procured from Component-Reagent (Russia). Silicon tetrachloride (STC) was acquired from Sigma-Aldrich (Germany).

2.2. Experimental setup

To produce copper and zinc oxide nanoparticles, the IFL setup was used as illustrated in Figure 1. This method comprises gas-phase nanoparticle synthesis, where the bulk sample is transformed into an atomic state, followed by atom condensation in the flow of an inert gas to generate nanoparticles. Within the quartz reactor near the induction levitation coil, a sample of the element either a cylinder or a wire ball approximately 0.5 g by weight to be processed was suspended. Subsequently, the entire gas system was vacuumed for several hours to achieve a high vacuum level, reducing any water traces in the system to below 5 ppm. After purging the system to eliminate impurities and moisture, it was pressurized with argon to the desired level (below 900 mbar), while maintaining the prescribed gas flow rate (15 L/min for copper and 15 L/min for zinc), regulated by a gas flow controller (Bronkhorst, the Netherlands). A high-frequency alternating current was applied to the inductor, then the sample melted and entered a levitated state without contacting the walls of the quartz reactor. Once the designated temperature was reached (1700°C for copper, 500°C for zinc), atoms evaporated from the surface, followed by condensing on the cooling gas upon reaching the crystallization point. This resulted in the formation of nanoparticles that constituted a jet stream, with density increasing alongside the temperature. As droplets evaporate, the wire of the same material continually replenishes, with the speed of this replenishment dictating the productivity over time. System setup comprises monitoring the temperature of the levitating droplet. Initially, the temperature increased until it reached a steady state, and then switched to the second collector, equipped with a filter cleaning system for prolonged system operation (Figure S1).

The initial material used for synthesizing ultrafine copper was a 0.2 mm wire with a purity of 99.9%. The levitation sample was prepared from 1.5 g by weight of the same wire. The achieved production rate was 3 g/h and synthesis was conducted at a temperature of 1740°C. Argon was used as the carrier gas at a flow rate of 15 L/min, while the system operated at a pressure of 200 mbar. To induce slight passivation of the nanoparticles, oxygen was introduced at a flow rate of 10 mL/min.

The starting materials for zinc oxide nanoparticles comprised granules weighing 1 g and a 0.5 mm wire with a purity of 99.9%. Synthesis was carried out at a pressure of 1 bar and the production rate was maintained at 10 g/h, with the levitating droplet temperature set at 820°C. Furthermore, due to the oxide layer present on the surface of the granules and wire, hydrogen was introduced into the system during setup to reduce the oxide film.

Moisture content in the vacuum system was monitored using a humidity sensor and mass spectrometer at m/z 18. The carrier gas flow rate was maintained at 15 L/min, with oxygen supplied to the side of the forming stream at a rate of 5 L/min. The SiO_2 substrate was synthesized using the sol-gel method within a polypropylene glycol matrix, utilizing silicon tetrachloride as the precursor for silica. The synthesis procedure is detailed in a previous publication (Vorotyntsev et al., 2020).

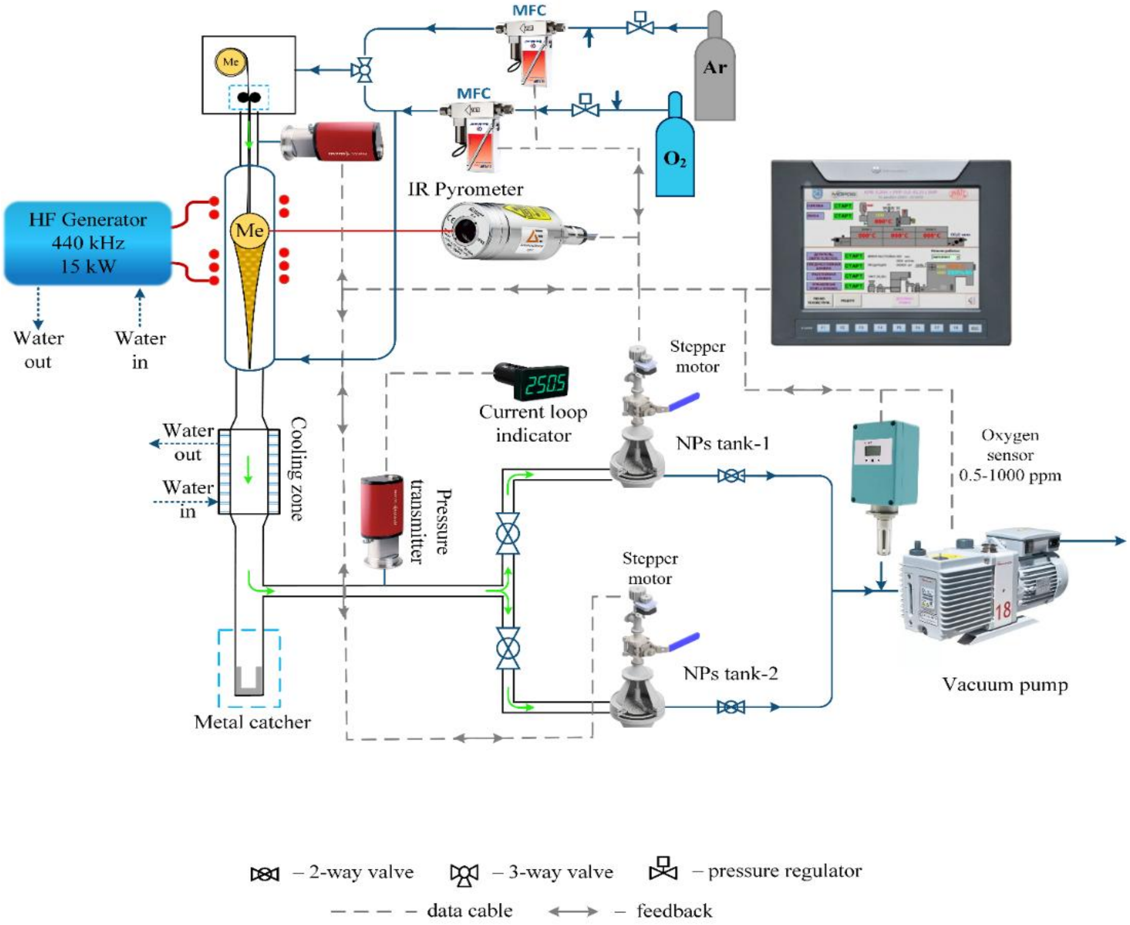

Figure 1 Experimental setup for obtaining nanoparticles

2.3. Preparation of the catalyst

To prepare Cu/ZnO/SiO_2 and Cu/SiO_2 catalyst, mechanochemical synthesis was used. Ultrafine powders were mixed in the exact proportions listed in Table 1 within an organic solvent (acetone), sonicated to achieve a homogeneous mixture, dried at 50°C, and then pressed to form tablets under a pressure of 100 bar.

Table 1 Composition of the obtained catalyst systems without filler

Sample	Cu mass fraction, %	ZnO mass fraction, %	SiO_2 mass fraction, %
Cu/SiO_2	10	-	90
Cu/ZnO/SiO_2	10	10	80

2.4. Physicochemical characterization

The physicochemical characteristics of the synthesized Cu, ZnO, and SiO_2 nanoparticles, as well as the catalytic systems Cu/SiO_2 and Cu/ZnO/SiO_2, were analyzed using various methods.

TEM was carried out on a LIBRA 200 MC Schottky Carl Zeiss AG (Germany) with a field emission gun operating at 200 kV and a resolution limit of 0.12 nm. Sample preparation was carried out by depositing the material on standard copper grids coated with a Formvar-shaped support grid of the Lacey type (200 mesh). Subsequently, nanoparticles in dry isopropyl alcohol were subjected to ultrasonic dispersion, before being transferred to ("fishing") onto TEM meshes.

For SEM, the samples were fixed on a sample holder using conductive carbon adhesive tape and coated with a 3 nm thick Au/Pd film by magnetron sputtering (Q150R S, Quorum, UK) to compensate for the electron beam-induced charge. The morphological and visual appearance characteristics were visualized by SEM (Merlin, Carl Zeiss, Germany) using in-lens secondary electron detector at 5–7 kV electron accelerating energy. The vacuum in a microscope chamber was ~10^{-6} mbar.

The phase composition of the synthesized nanoparticles was confirmed through X XRD analysis (Shimadzu XRD-7000, Japan). Measurements were carried out at 40 kV and 30 mA. The scattering slit RS of the detector was 0.3 mm wide and the exposure was conducted within the angular range of 10 – 80° (2θ). The scanning step was 0.02°, with an exposure time of 0.5 s at each step.

For nanoparticle purity analysis, an inductively coupled plasma mass spectrometer ELAN 9000 (PerkinElmer) was used. The nanoparticles obtained were dissolved in concentrated nitric acid at a concentration of 1 µg/L using a fully automated semi-quantitative analysis, known as the TotalQuant method for PerkinElmer instrument.

The specific surface area and pore size distribution were determined using adsorption/desorption isotherms recorded on the Autosorb IQ instrument (Quantachrome Instruments, USA) after previous sample pretreatment.

TPO, TPR, and TPD experiments were conducted using the Autosorb IQ instrument (Quantachrome Instruments, USA). The TPR of the freshly prepared catalyst was conducted in a 5% H_2/Ar flow. Initially, 0.3 g of the catalyst was loaded into a flow cell and purged with argon at 200°C (heating rate of 20°C/min) for 1 hour at a flow rate of 30 mL/min. After cooling the cell to 50°C, the sample was saturated with 5% H_2/Ar for 30 minutes at a flow rate of 30 mL/min to stabilize the baseline signal. The reduction process was carried out within the temperature range of 50-800°C (heating rate of 10°C/min). A thermal conductivity detector (TCD) was then used to monitor changes in hydrogen concentration within the flow. At 800°C and a signal plateau, a pulse injection of a fixed volume of pure hydrogen was administered to assess the area under the TPD-H_2 curve.

The TPO of the Cu/SiO_2 and Cu/ZnO/SiO_2 catalyst was conducted using a 5% O_2/Ar flow. Initially, 0.3 g of the catalyst was placed into a flow cell and purged with argon at 200°C (heating rate of 20°C/min) for 1 hour at a flow rate of 30 mL/min to remove moisture. After cooling the ampoule to 50°C, the sample was saturated with 5% O_2/Ar for 30 minutes at a flow rate of 30 mL/min to stabilize the baseline signal. The oxidation of the catalyst was performed within the temperature range of 50-500°C (heating rate of 10°C/min). A TCD was used to monitor changes in oxygen concentration within the flow. At 500°C and a signal plateau, a pulse injection of a fixed volume of pure oxygen was introduced to evaluate the area under the TPO-O_2 curve.

Following complete oxidation, TPD with hydrogen was conducted to assess the amount of metallic phase. TPD was performed for 0.3 g of the Cu/SiO_2 and Cu/ZnO/SiO_2 catalyst. Initially, the catalyst were reduced in a 5% H_2/Ar atmosphere for 2 hours at 250°C and then purged with Ar at a flow rate of 60 mL/min at 300°C (with a heating rate of 20°C/min) for 1 hour. The samples were cooled to 50°C and saturated with H_2 or CO_2 at a flow rate of 50 mL/min for 1 hour. Following saturation, the remaining H_2 or CO_2 was purged with argon, and desorption of H_2 or CO_2 was carried out up to 600°C with a heating rate of 10°C/min.

3. Results and Discussion

3.1. Characterization of the obtained copper and zinc oxide particles and the silica substrate

The physicochemical characterization of the obtained porous SiO_2 substrate, Cu, and ZnO nanoparticles was performed using SEM. Figure 2 shows microphotographs of the obtained samples along with elemental analysis of these areas. SEM microphotograph of porous SiO_2 substrate calcined at 500°C (Figure 2A), shows that the powder consists of spherical, densely interconnected agglomerated nanoparticles with an average size of 10 nm, formed on the fluctuation grid of polyethylene glycol macromolecules. The elemental analysis of the substrate (Figure 2B) demonstrates the presence of Si and O in a stoichiometric atomic ratio of 1:2. Moreover, the absence of carbon indicates that the polyethylene glycol burned during annealing in the muffle furnace.

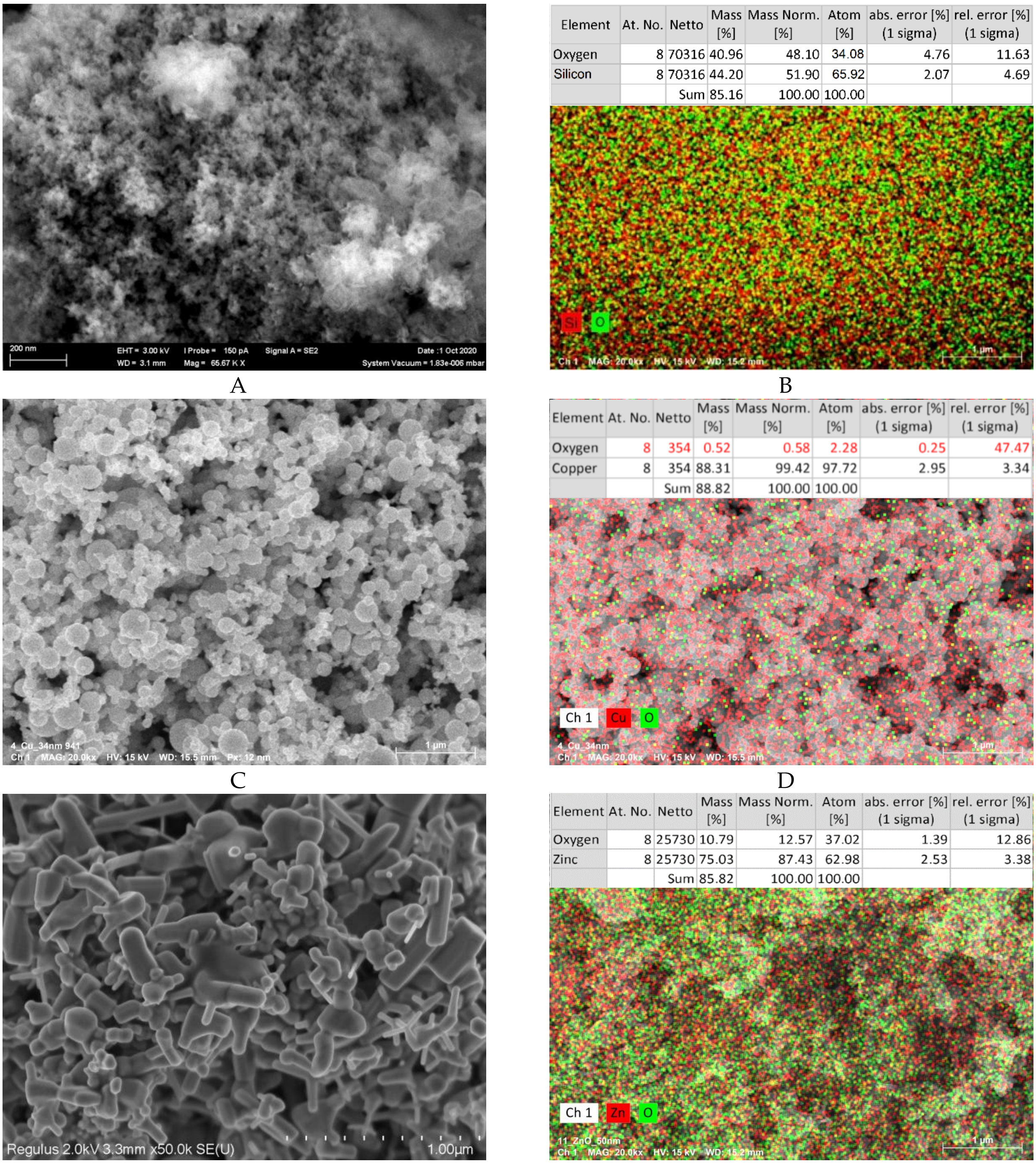

A

Element	At. No.	Netto	Mass [%]	Mass Norm. [%]	Atom [%]	abs. error [%] (1 sigma)	rel. error [%] (1 sigma)
Oxygen	8	70316	40.96	48.10	34.08	4.76	11.63
Silicon	8	70316	44.20	51.90	65.92	2.07	4.69
		Sum	85.16	100.00	100.00		

B

C

Element	At. No.	Netto	Mass [%]	Mass Norm. [%]	Atom [%]	abs. error [%] (1 sigma)	rel. error [%] (1 sigma)
Oxygen	8	354	0.52	0.58	2.28	0.25	47.47
Copper	8	354	88.31	99.42	97.72	2.95	3.34
		Sum	88.82	100.00	100.00		

D

E

Element	At. No.	Netto	Mass [%]	Mass Norm. [%]	Atom [%]	abs. error [%] (1 sigma)	rel. error [%] (1 sigma)
Oxygen	8	25730	10.79	12.57	37.02	1.39	12.86
Zinc	8	25730	75.03	87.43	62.98	2.53	3.38
		Sum	85.82	100.00	100.00		

F

Figure 2 SEM and SEM-EDS Microphotographs: A - SEM SiO_2, B - SEM-EDS SiO_2, C - SEM NPs Cu, D - SEM-EDS NPs Cu, E - SEM NPs ZnO, F - SEM-EDS ZnO

SEM microphotographs depicting copper nanoparticles and the size distribution are depicted in Figure 2C. The microphotographs show that the copper samples consist of loosely aggregated ultrafine particles with a spherical morphology. Statistical analysis of the microphotographs indicated an average particle size of 64 nm. Figure 2D shows the SEM-EDS analysis of the selected region for copper nanoparticles. Background peak values remained consistent within the margin of error, necessitating the subtraction. Apart from the adsorbed oxygen on the surface, an oxide phase might have formed on the ultrafine particles surface. However, the obtained values are minimal and fall within the error range. This can be inferred based on the copper ultrafine sample, where the oxygen concentration does not exceed 2.28 atomic %. The microphotographs in Figure 2E show the morphology of ultrafine ZnO represented as nanorods with a length of 118 nm and a diameter of approximately 63 nm. The SEM-EDS results for zinc oxide (Figure 2F) suggested that there are impurities in the form of pure zinc nanoparticles on the surface, confirmed by the presence of a phase in the XRD results.

The phase composition determined by XRD for the Cu and ZnO nanoparticles and porous SiO_2 substrate is depicted in Figure 3. More specifically, Figure 3A shows the X-ray diffractogram of the Cu nanoparticles. Relative to the copper standard (PDF № 04-0836), characteristic diffraction peaks of copper were observed at $2\theta = 43.3°$, 50.4°, and 74.1°. These peaks correspond to the facets (111), (200), and (220) of the face-centered cubic (FCC) structure. Figure 3B shows the X-ray diffractogram of the zinc oxide nanoparticles. The diffraction peaks located at $2\theta = 31.77°$, 34.42°, 36.25°, 47.54°, 56.6°, 62.86°, 66.37°, 67.96°, 69°, 72.66°, 76.95°, 81.36°, and 89.6° corresponding to the facets (100), (002), (101), (102), (110), (103), (200), (112), (201), (004), (202), (104), and (203) are clearly indexed as the hexagonal wurtzite phase (structural type P63/mc) of ZnO according to the data from PDF № 36-1451.

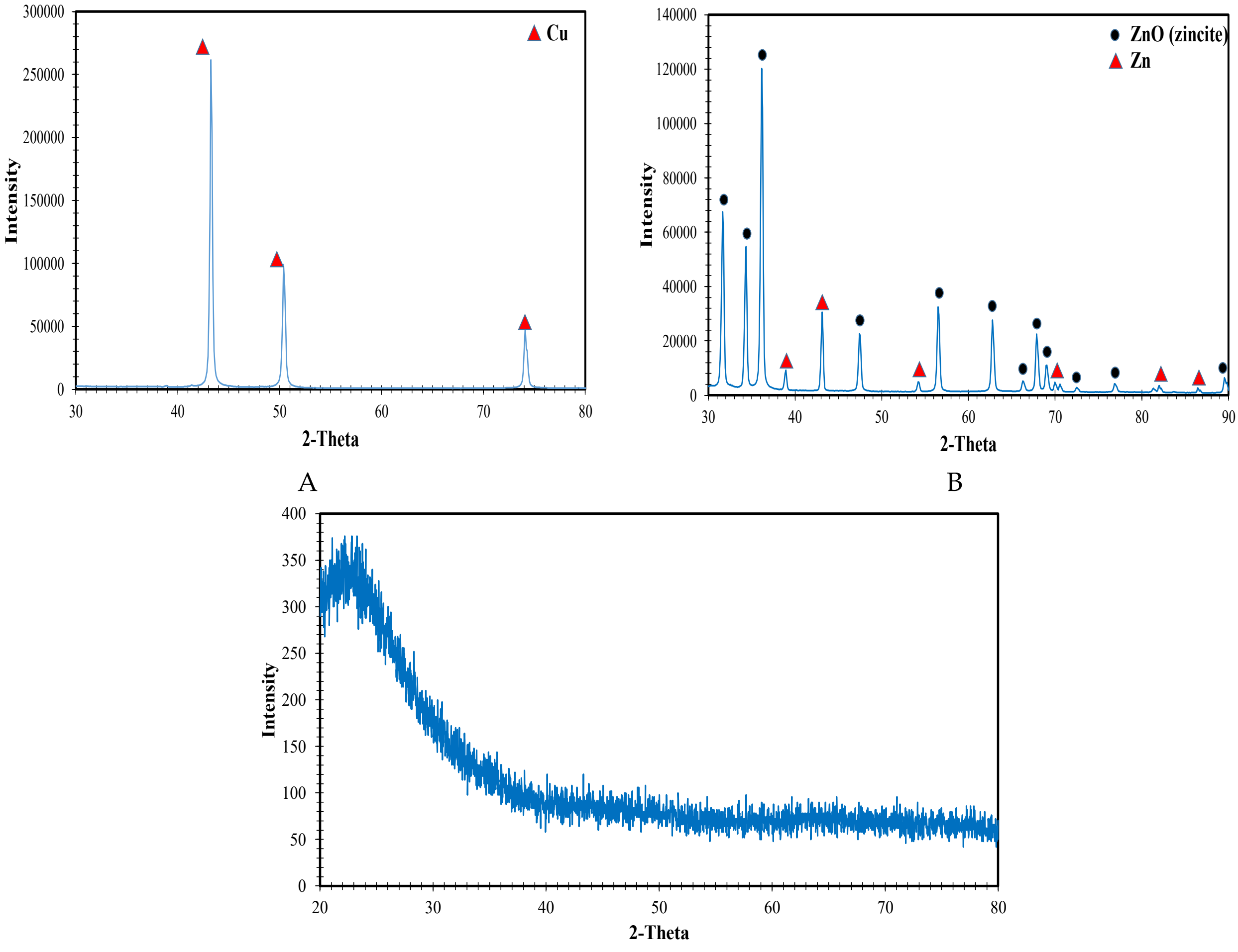

A

B

C

Figure 3 XRD patterns of NPs and powder: A - Cu, B - ZnO, C – SiO_2

Additionally, the X-ray diffractogram shows peaks at 2θ = 39°, 43.23°, 54.33°, 70.05°, 70.66°, 82.1°, and 86.55° corresponding to the lattice facets (100), (101), (102), (103), (110), (112), and (201) of zinc, according to the data from PDF № 04-0831. Figure 3C shows the characteristic X-ray diffractogram of amorphous SiO_2 powder. Based on the diffraction patterns and the Scherrer equation (see equation 1), the average crystallite size was calculated using the formula:

$$d = \frac{K\lambda}{\beta cos\theta} \qquad (1)$$

Where d - average crystallite size, K - Scherrer's constant (K = 0.94), λ - X-ray radiation wavelength (CuKα radiation wavelength 0.15418 nm), β - width of the reflection at half-height of the peak, and θ - diffraction angle. The calculation results are presented in Table 2.

The TEM microphotographs obtained for copper and zinc oxide nanoparticles (Figure 4) were subjected to statistical analysis to determine the distribution of nanoparticles by size. For copper (Figure 4A), the formation of chain-like agglomerates and aggregates with strong bonding between ultrafine particles (UFPs) is clearly visible, which remains intact during ultrasonic treatment. The average particle size according to TEM results is 70 nm. Additionally, individual copper ultrafine particles with a size of 10 nm were observed. CBED pattern unambiguously demonstrated that the core of the particle was fcc-Cu in orientation [323]. After indexing the selected area electron diffraction (SAED) pattern (Figure 4B), diffraction rings corresponding to copper facets (111), (200), (220), (400), (311), (420), and (422) were observed, according to PDF № 04-0836. The characteristic rings of the monoclinic Cu_2O phase with parameters a=4.6833(2) Å, b=3.4208(1) Å, c= 5.1294(2) Å, and β=99.567(1) were also present. The observed nanoparticles of the zinc oxide (Figure 4C) in the TEM microphotograph predominantly appear as nanorods with an average length of 109 nm and a diameter of 54 nm. In the case of the other samples, the observed nanoparticles appear as spheres, forming weakly bonded agglomerates. Figure 4D represents a diffraction pattern obtained for the zinc oxide sample. From this pattern, facets (100), (002), (102), (110), (201), (202), (104), (203), (211), (212), (213), and (220) corresponding to zinc oxide were identified according to PDF № 36-1451. Additionally, diffraction rings from facets (100), (101), (102), and (211) of pure zinc were detected (PDF № 04-0831).

Figure S2 represents the Energy Dispersive X-ray analysis (EDXS) of Cu and ZnO nanoparticles. Comparative analysis with the data obtained from SEM-EDS allows the assessment of the oxidation degree within the nanoparticles. In the case of copper nanoparticles, the oxygen content remained unchanged, likely indicating oxide formation on the surface during sample preparation. The relatively high copper content may be attributed to the fluorescence of the copper grid on which the sample was deposited. For ZnO nanoparticles, the zinc content obtained from the EDXS analysis increased, suggesting incomplete oxidation during synthesis. Additionally, significant particle decomposition under the electron beam was observed for ZnO.

The synthesized Cu, ZnO, and SiO_2 nanopowders were investigated using the low-temperature nitrogen adsorption method at 77 K. The porometry results and the average particle diameter obtained by other methods (SEM, TEM, XRD, DLS) are presented in Table 2. Given that nanoparticles show a spherical morphology, the mean particle diameter can be calculated using the specific surface area. The specific surface area was determined using the BET method. Considering the specific surface area and assuming that nanoparticles have a spherical shape, the formula for estimating the average nanoparticle diameter can be applied (Equation 2):

$$\langle D\rangle_{BET} = \frac{6}{S\rho} \qquad (2)$$

where ρ is the material density in g/cm^3, $m = (4\pi/3)R^3P$, and $S = 4\pi R^2$, where πR represents the radius of the particle. However, due to the tendency of nanoparticles to agglomerate, the average size is usually more significant than that obtained by statistical processing of SEM or TEM images, indicating strong particle bonding in the agglomerate.

The adsorption-desorption isotherms obtained for Cu and ZnO nanoparticles show identical shapes. Figures 5A and 5B show a typical adsorption/desorption isotherm characteristic of nanoparticles. The resulting curve corresponds to Type III isotherm, which is typical for nonporous sorbents with low adsorbate-adsorbent interaction energy. This type of isotherm signifies free monolayer adsorption. The slight inflection point observed around a relative pressure of 0.15 is attributed to increased adsorbate-adsorbate interaction compared to adsorbate-adsorbent interaction. The observed hysteresis between the adsorption and desorption isotherms suggests the presence of mesopores. This type of hysteresis corresponds to Type A and is indicative of cylindrical pores. The isotherm for the silica substrate (Figure 5C) corresponds to Type 4, characteristic of porous sorbents predominantly containing micro- and mesopores. Type A hysteresis is associated with cylindrical-shaped pores.

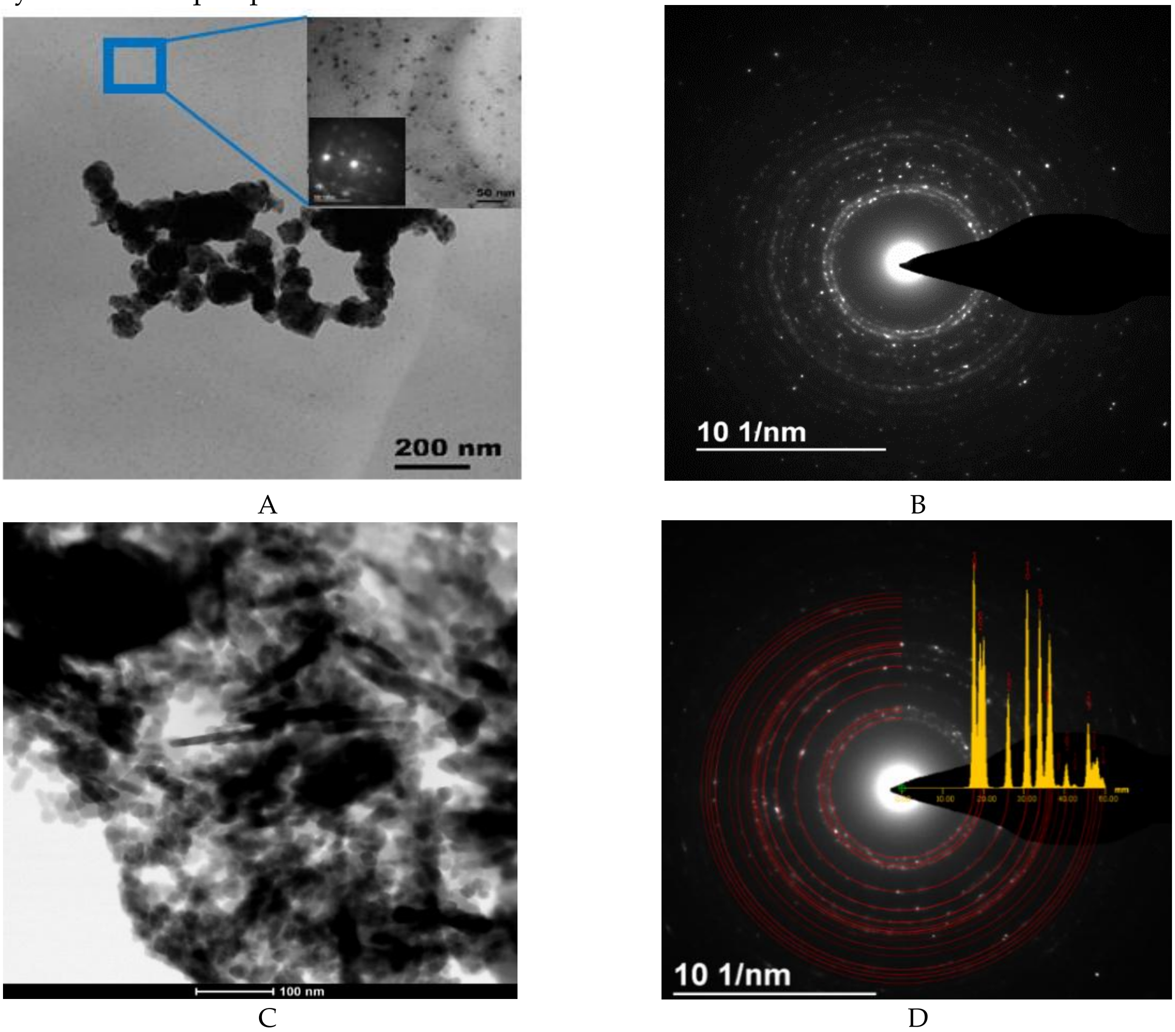

A B

C D

Figure 4 TEM micrograph of NPs and particle size distribution, SAED diagram: A, B – Cu, C, D – ZnO

Table 2 Structural characteristics of nanoparticles according to the data of low-temperature adsorption of nitrogen at 77 K and the ASPS (<D>$_{BET}$) of the resulting particles

Sample	S_{BET}, m$_2$/g	V_{Pore}, cm$_3$/g	<D>$_{Pore}$, nm	<D>$_{BET}$, nm	<D>$_{TEM}$, nm	<D>$_{SEM}$, nm	<D>$_{XRD}$, nm
Cu	23	0.073	2.453	29	64	70	26
ZnO	11	0.039	2.449	94	62/109	54/118	85
SiO_2	567	0.454	1.425	4	-	10	-

The resulting nanoparticle purity was evaluated using ICP-MS. The IFL method allows for obtaining nanoparticles without adding other impurities. The non-contact nature of sample heating and the single-stage process contribute to achieving high purity, in contrast to methods requiring the use of a crucible, which can reduce product purity due to the aggressive nature of molten metal. The purity declared by the manufacturer for the zinc and copper wires was 99.9%. The results of ICP-MS showed that the actual purity for the copper wire was 99.84% and for the zinc wire was 99.95%, significantly lower than the values claimed by the manufacturer. Based on the analysis of the obtained nanoparticles, the copper ultrafine particles possess a purity of 4N2 (99.992%), while the zinc oxide ultrafine particles have a purity of 4N5 (99.995%), with the concentration of other elements being less than 50 ppm. The impurity compositions of the original zinc sample compared to those of the zinc nanoparticles indicate a significantly higher level of purity in the latter. This observation suggests minimal additional contamination during the high-temperature synthesis of the ultrafine particles. Furthermore, thermodistillation occurs during the process, where elements with high segregation coefficients remain in the molten levitating droplet and do not evaporate. This phenomenon is evident in both the synthesis of copper ultrafine particles and ZnO.

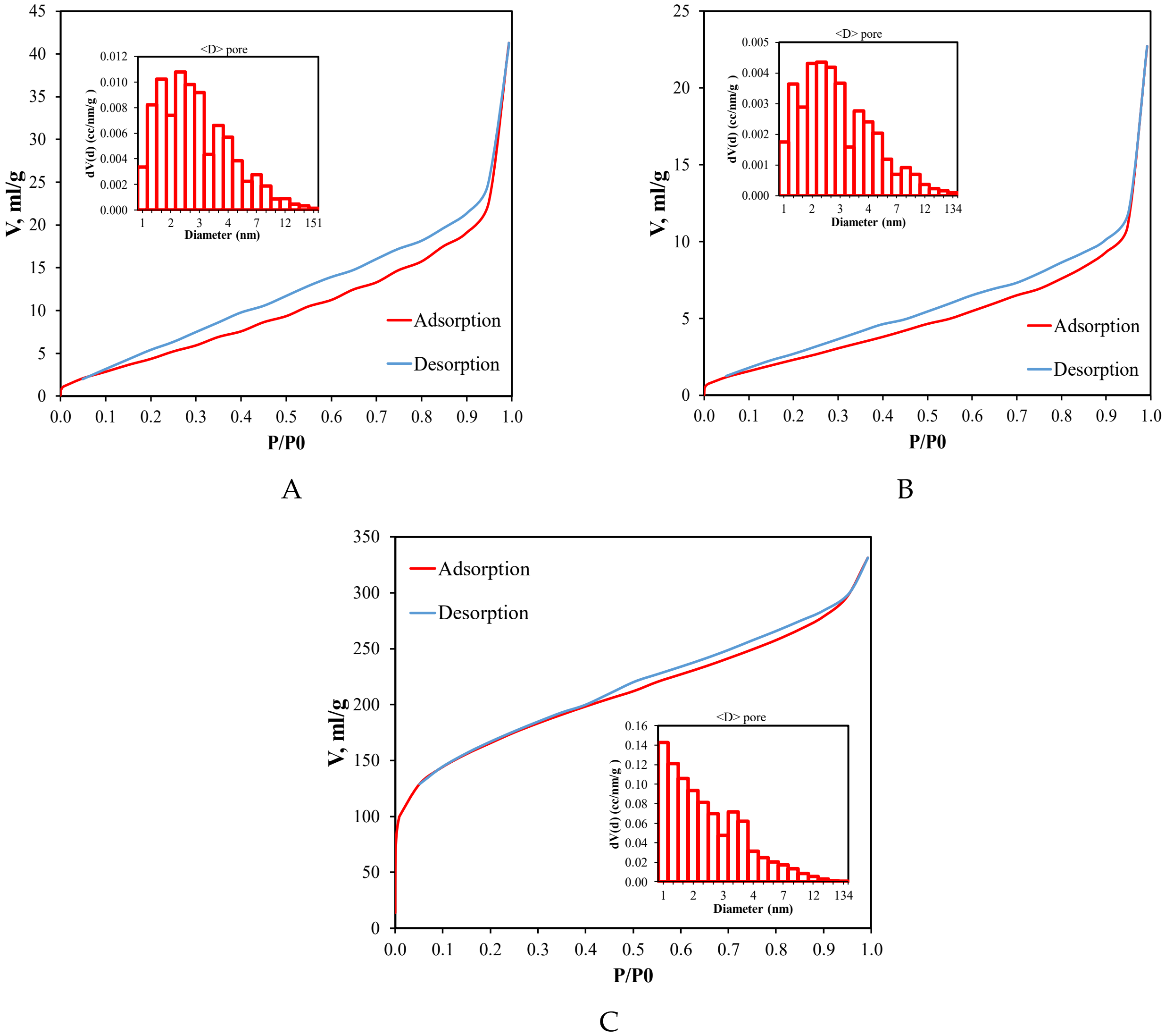

A

B

C

Figure 5 Adsorption-desorption isotherm (N_2, 77 K): A – Cu, B – ZnO, C - SiO_2

3.2. Characterization of the catalyst

The physicochemical characterization of the obtained Cu/SiO_2 and Cu/ZnO/SiO_2 catalyst was conducted using TEM, TEM-EDX, XRD, and low-temperature porosimetry methods. High-resolution TEM micrographs (Figure 6) show catalyst prepared using mechanochemical methods, with Figure 6A representing the $Cu/ZnO/SiO_2$ catalyst system. Electron diffraction from selected areas showed that the system comprises a SiO_2 substrate, copper nanoparticles with a size of 70 nm, and a fragment of ZnO nanoparticles with a size of 17 nm. Figure 6B shows a micrograph of the Cu/SiO_2 catalyst, illustrating the SiO_2 substrate with copper nanoparticles sized at 34 nm. FFT depicts the red square (up) and simulated electron diffraction pattern CuO (below) (axis of the zone [021]). The pattern obtained from the yellow square corresponds to ZnO (S.G. P63/mmc) in [100] zone axis. The FFT model in green shows SiO_2 in an amorphous phase.

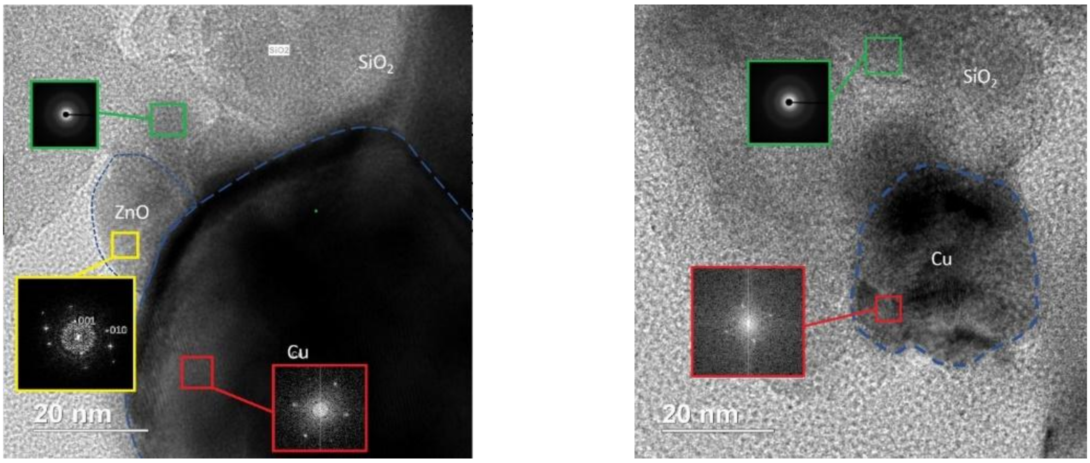

A B

Figure 6 TEM micrographs of the obtained catalytic systems: A - $Cu/ZnO/SiO_2$, B - Cu/SiO_2

FFT shows the red square (up) and simulated electron diffraction pattern CuO (below) (axis of the zone [021]). The uniformity of the silicon substrate coverage with Cu and ZnO nanoparticles was investigated using TEM-EDX. Figure S3 depicts the EDXS results, showing that in both cases, there is a uniform coating of the silicon substrate. This is unexpected when preparing catalyst through mechanochemical methods. The phenomenon is likely attributed to the specific mixing method used, comprising ultrasonic dispersion with top immersion up to complete evaporation of the organic solvent. This approach prevents the segregation and precipitation of components within the prepared SiO_2 system.

The obtained catalyst were studied by X-ray phase analysis. Figure S4 shows the X-ray diffractograms of the catalyst. The diffractogram for the $Cu/ZnO/SiO_2$ sample demonstrates the presence of peaks corresponding to the Cu and ZnO phases. From the diffractogram, only the Cu phase is clearly visible. The porosity of the obtained catalyst was examined to evaluate the specific surface area of the substrate following deposition. Table 3 shows that the addition of 10 wt.% copper nanoparticles to the substrate led to a reduction in the specific surface area by approximately 22% while incorporating 10 wt.% Cu and 10 wt.% ZnO nanoparticles resulted in a 40% decrease in the specific surface area of the catalyst compared to the initial substrate. The average pore diameter remained unchanged within the instrument margin of error. The reduction in pore volume is caused by the contribution of the active components to the specific surface area of silica and the occlusion of macropores during mechanochemical synthesis.

Table 3 Structural characteristics of the catalytic systems Cu/SiO_2, $Cu/ZnO/SiO_2$ obtained by low-temperature porometry

Sample	S_{BET}, m^2/g	V_{Pore}, cm^3/g	$<D>_{Pore}$, nm
SiO_2	567	0.4	1.425
Cu/SiO_2	441	0.32	1.428
$Cu/ZnO/SiO_2$	349	0.25	1.427

The isotherms obtained for Cu/SiO_2 and Cu/ZnO/SiO_2 in Figure S5, similar to the substrate, also show characteristics of Type 4 isotherms, typical for porous sorbents. However, in the inflection region of the isotherm between 0.1 and 0.5, an earlier plateau onset compared to the pure substrate was observed, indicating a reduction in meso- and macropores. The pore size distribution remains unchanged and falls within the instrument error. Adsorption and activation of CO_2 by copper-based catalyst are important steps in methanol synthesis, which characterize the catalyst activity. Figure 7A shows the TPD curves of CO_2 for Cu/SiO_2 and Cu/ZnO/SiO_2 catalyst. The graph depicts three CO_2 desorption peaks and all profiles can be deconvoluted into three Gaussian peaks corresponding to weak (α-peak), moderate (β-peak), and strong (γ-peak) adsorption sites at approximately 150, 430, and 560°C, respectively (Jangam et al., 2021; Gao et al., 2013). The integrated peak areas of α, β, and γ peaks are presented in Table 4. The desorption peak temperature represents the strength of adsorbed CO_2, while the integrated peak area represents the amount of CO_2 adsorbed per unit mass of the catalyst.

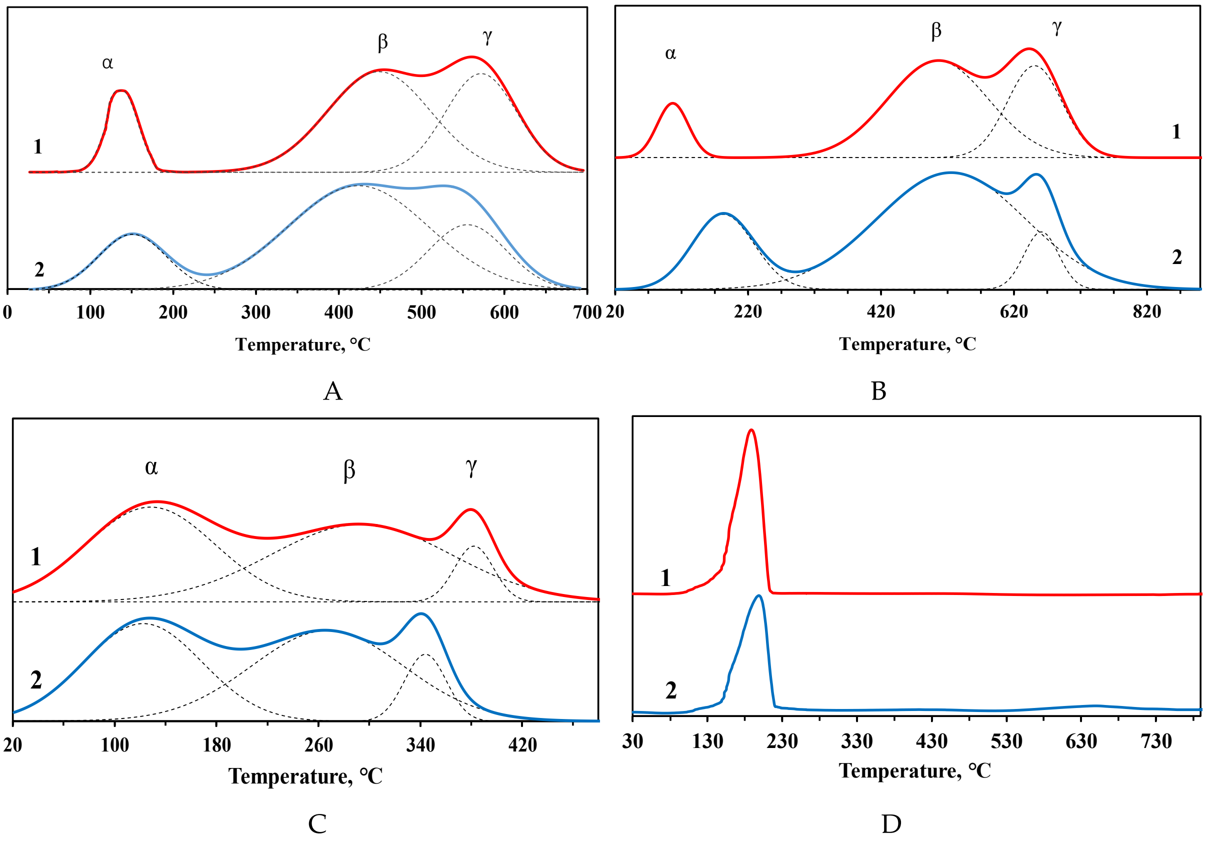

Figure 7 TPx profiles for pre-reduced catalyst: A - CO_2-TPD, B - H_2-TPD, C - TPO-O_2, D - H_2-TPR of fully oxidized catalyst (TPO). 1 - Cu/SiO_2, 2 - Cu/ZnO/SiO_2

Based on the data in Table 4, the quantity of desorbed carbon dioxide on weakly basic sites increased twice with the addition of zinc oxide to the catalytic system, likely attributable to the robust physical adsorption of CO_2 on the metal oxide. A similar pattern was observed on the β-basic sites. With increasing temperature, the contribution to the sorption capacity of zinc oxide diminished, suggesting the absence of chemical adsorption using the Cu/ZnO nanoparticles, positively impacting catalyst poisoning. Consequently, the incorporation of ZnO enhances the adsorption of CO_2 on the catalyst surface, theoretically augmenting conversion rates, without additional chemical adsorption, which directly influences selectivity towards CO_2.

The interaction of weakly basic sites with CO_2 (α-peaks at 140-155°C) leads to the formation of bicarbonate, which shows resistance to hydration and readily desorbs, subsequently converting into CO_2 (Jiang et al., 2023). High-temperature desorption peaks around 430°C (β-peak) and 560°C (γ-peak), corresponding to moderate and strong basic sites, respectively. Moderately strong basic sites on the catalyst surface are associated with metal-oxygen pairs (Cu-O, Zn-O) and low-coordinated oxygen ions (O^{2-}) (Jiang et al., 2023; Yang et al., 2016). CuO possesses a single pair of electrons available for exchange, while the CO_2 molecule carries a positive charge on the carbon atom, capable of interacting with the electron pair (Shawabkeh et al., 2022). On the β and γ basic sites, adsorbed CO_2 undergoes stepwise hydrogenation by dissociated hydrogen atoms, leading to the formation of HCOO, H_2COO, H_2COOH, and H_2CO. The C=O bond in H_2CO absorbed on strongly basic sites (γ) is activated by surface hydrogen atoms to form methanol, due to the strong C-γ bond. However, the same bond absorbed on β-sites remains relatively stable due to the weak C-β bond, resulting in the dehydrogenation of H_2CO to CO. This implies that the intermediate product H_2CO, formed through the formate pathway, can be converted not only to methanol but also CO (Gao et al., 2013).

To obtain useful information about active sites, clear and reproducible data were obtained using O_2-TPO (Figure 7C). The TPO signal consists of three peaks, attributed to stepwise oxidation, including surface monolayer nanoparticles from Cu^0 to Cu^+, bulk oxidation to Cu^+, and oxidation to the higher oxide phase CuO from Cu^+ to Cu^{2+} (Zhao et al., 2013). Table 6 shows data on the quantity of absorbed oxygen up to complete oxidation of the copper catalyst. Based on the results, there was a slight increase in the amount of oxygen needed for the complete oxidation of the catalyst with the addition of ZnO. This increase is likely attributed to the oxidation of impurity zinc nanoparticles observed during scanning methods.

Table 4 Areas of the α, β, γ peaks on the H_2-TPD curve for Cu/SiO_2 and $Cu/ZnO/SiO_2$ catalyst (mmol/g)

Sample	H_2-TPD, mmol/g			
	α-peak	β-peak	γ-peak	Sum
Cu/SiO_2	0.551	3.192	1.647	5.543
$Cu/ZnO/SiO_2$	1.090	4.077	0.469	5.739

Experiments on hydrogen temperature-programmed reduction (H_2-TPR) were conducted for both Cu/SiO_2 and $Cu/ZnO/SiO_2$ catalyst, previously fully oxidized in TPO-O_2 experiments, and the results are presented in Figure 7D. H_2-TPR was used to ascertain the most effective catalyst reduction temperature. The reduction peak in the temperature range of 190°C to 200°C can be attributed to the decrease in highly dispersed CuO (Ou et al., 2023). This is in line with another study stating that low copper reduction temperature on the catalyst may be due to the low nanoparticle dispersion (Kong et al., 2023). In the $Cu/ZnO/SiO_2$ sample, a broad reduction peak occurred at around 650°C, corresponding to the reduction of ZnO. However, in the XRD pattern of the $Cu/ZnO/SiO_2$ sample (Figure S6), no reflections of ZnO or metallic zinc phases were observed after the experiment. The absence of zinc-containing phases is because at temperatures above 420°C, metallic zinc transitions to a molten state, with the reduction process of ZnO starting at 530°C, and the reduced product sublimated and condensed in the cold part of the flowing analyzed cell (Qi and Hu, 2020).

Table 5 Areas of the α, β, γ peaks on the O_2-TPO curve for Cu/SiO_2 and $Cu/ZnO/SiO_2$ catalyst (mmol/g)

Sample	O_2-TPO, mmol/g			
	α-peak	β-peak	γ-peak	Sum
Cu/SiO_2	11.390	13.291	2.073	22.622
$Cu/ZnO/SiO_2$	10.589	12.778	2.590	24.512

3.3. The catalytic properties of Cu/SiO_2 and $Cu/ZnO/SiO_2$ catalyst for CO_2 hydrogenation processes

The synthesis of methanol is essential in the process of CO_2 hydrogenation, given the potential as a feedstock in the chemical industry and alternative to fossil fuels, including methanol fuel cells. Consequently, this study aimed to develop a highly active and selective catalyst for methanol synthesis. Commercial catalyst using Cu and Zn have demonstrated significant selectivity towards methanol and yield satisfactory results.

The efficacy of CO_2 hydrogenation catalyst was assessed using a catalytic setup (Figure S7) with a fixed-bed system. The tubular reactor featured an internal and external diameter of 5 mm and 10 mm respectively. Before loading into the reactor, the catalyst was granulated to a size of 20 mesh. To achieve this, 3 g of catalyst with a bed length of 10 cm, was loaded in the reactor and reduced in a stream of a 5% hydrogen mixture in argon at 230°C for 2 hours under atmospheric pressure. After pre-reduction, the catalyst bed was cooled to room temperature. A reaction mixture of $H_2:CO_2 = 3:1$ was introduced into the reactor at a flow rate of 350 mL/min. This flow rate was selected to ensure a gas-catalyst contact time of 0.5 seconds. To maintain a constant flow rate, a high-pressure mass flow controller (Bronkhorst) was used. The pressure in the reactor was regulated by an automatic back-pressure regulator.

The experiment was conducted under four different pressure conditions including 0.5, 1, 3, and 5 MPa. For each trial, a fresh catalyst was loaded into the reactor and tested across various temperatures ranging from 150 to 300°C. Data points were collected during steady-state reaction conditions at the specified temperature and pressure. Moreover, no catalyst deactivation was observed during the experiment. The initial feed mixture comprised 30% CO_2 and 70% H_2. To prevent liquid phase condensation, all gas lines from the reactor to the mass spectrometer were heated to 100°C. The CO_2 conversion was determined based on the concentration at the reactor outlet. Conversion and product selectivity values were computed by averaging multiple inputs after stabilizing the product concentration. The standard deviations of conversion and product selectivity were <1%.

In the assessment of the synthesized nanoparticles, the catalytic efficacy of $Cu/ZnO/SiO_2$ and Cu/SiO_2 catalyst in CO_2 hydrogenation was examined. Figure 8 A shows the CO_2 conversion rates obtained at various temperatures (150-300°C) and pressures (0.5-5 MPa). Elevated CO_2 conversion rates were observed at higher pressures and temperatures for both catalyst. The catalyst incorporating ZnO nanoparticles demonstrated superior efficiency and the maximum CO_2 conversion achieved was 30.1% at 5 MPa and 300°C. During the experiments, carbon monoxide, methanol, ethanol, methyl formate, dimethyl ether, propanol, isobutyl, and isopropanol were identified.

Figure 8 B shows the relationship between methanol selectivity and pressure as well as temperature. The highest methanol selectivity was observed at low temperatures and pressures exceeding 1 MPa. Increasing pressure resulted in higher methanol selectivity and CO_2 conversion, as depicted in Figure 8 B, leading to enhanced methanol productivity. At pressures of 0.5 and 1 MPa, temperature variations had negligible effects on methanol selectivity. However, at pressures of 3 and 5 MPa, increasing temperature reduced methanol selectivity, although productivity increased due to the heightened activity of the catalytic reaction. The maximum methanol yield of 108 $mg/g_{cat}{\cdot}h$ was attained at 280°C and 5 MPa. The incorporation of zinc oxide augmented methanol selectivity at lower temperatures by 2-16% (depending on pressure) but gradually declined to 2% with rising temperature. The selectivity towards CO increased with temperature, as expected due to the endothermic nature of the reaction.

The addition of zinc oxide did not induce significant changes in the CO selectivity difference. When the reaction temperature increased from 150 to 280°C, there was an approximately 15-, 71-, 146-, and 28-fold increase in CO productivity at 0.5, 1, 3, and 5 MPa, respectively. Furthermore, pressure did not exert a significant influence on the catalytic reaction compared to temperature. Methyl formate formation occurred at pressures above 1 MPa. Further pressure increases enhanced the selectivity towards methyl formate, reaching a maximum value of 3.1% at 5 MPa and 280°C. However, raising the temperature above 300°C led to a plateau in methyl formate formation. The highest selectivity towards ethanol was 0.04% at 260°C and 5 MPa. The selectivity towards methyl formate and propanol was not more than 0.01% at 250°C, while for isopropanol, it was not more than 0.005% at 250°C.

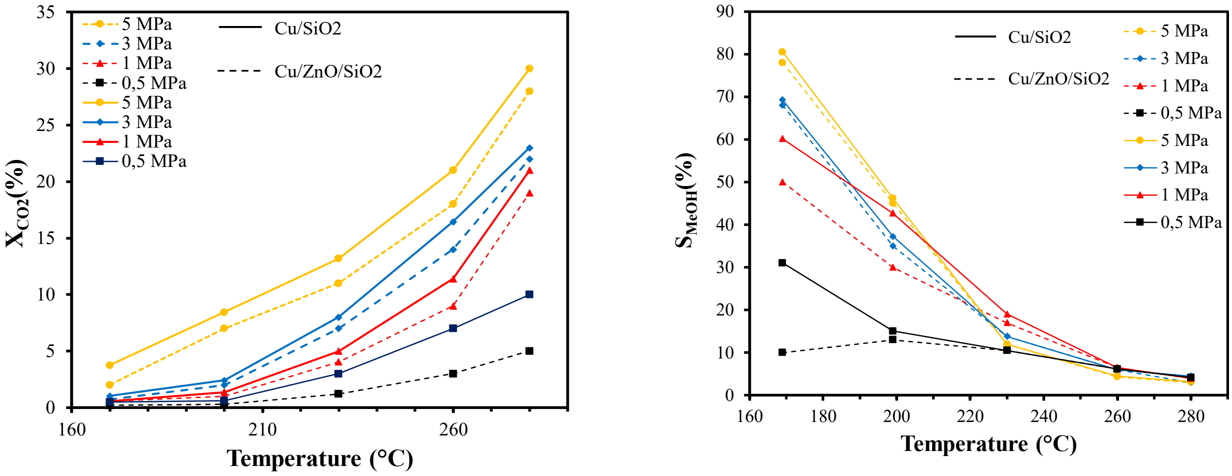

A B

Figure 8 A - CO_2 conversion as a function of temperature on Cu/SiO_2 and $Cu/ZnO/SiO_2$ in an H_2:CO_2 mixture = 3:1 at pressures of 0.5, 1, 3, 5 MPa; B - Methanol selectivity on Cu/SiO_2 and $Cu/ZnO/SiO_2$ in the H_2:CO_2 = 3:1 mixture at pressures of 0.5, 1, 3, 5 MPa

As anticipated, the reaction temperature influenced catalytic efficiency. Experimental results indicate that low temperature and high pressure were favorable for methanol synthesis using the $Cu/ZnO/SiO_2$ catalyst obtained through the induction flux levitation method. The formation of dimethyl ether on $Cu/ZnO/SiO_2$ due to methanol dehydration decreased at 5 MPa.

4. Conclusions

In conclusion, Cu and ZnO nanoparticles were synthesized using the induction levitation technology. The morphology was examined through TEM and SEM methods, showing that the Cu nanoparticles formed aggregates with an average size of approximately 65 nm, with individual particles measuring less than 10 nm. ZnO, synthesized in the form of nanorods, had dimensions of 62/109 nm. XRD, SEM-EDS, and TEM-EDX analyses indicated that the Cu nanoparticles lacked an oxide phase, while ZnO showed the presence of underoxidized metallic zinc. The size and surface structural properties of the particles were determined through low-temperature porometry. The purity of the Cu and ZnO nanoparticles was assessed using ICP-MS, which showed purity levels of 99.992% and 99.995%, respectively, surpassing those of the initial materials. A mesoporous substrate for catalyst was obtained through the sol-gel method, in which SiO_2 was derived from $SiCl_4$, with polyethylene glycol acting as the structure-directing agent. Surface characteristics were assessed using low-temperature porosimetry, which showed a specific surface area of 567 m^2/g. The catalyst Cu/SiO_2 and $Cu/ZnO/SiO_2$ were prepared by mechanochemical synthesis, with specific surface areas of 441 and 349 m^2/g, respectively. TEM-EDX showed a uniform distribution of nanoparticles on the substrate. Furthermore, thermoprogrammed desorption indicated that the addition of ZnO nanoparticles increased the physical sorption of CO_2 and H_2, affecting the conversion of CO_2. The temperature for catalyst reduction by hydrogen was determined by TPR, which ranged from 190°C to 200°C, indicating low nanoparticle dispersion. The catalytic activity of $Cu/ZnO/SiO_2$ and Cu/SiO_2 catalyst in CO_2 hydrogenation was assessed using a fixed-bed flow system at temperatures ranging from 150 to 300°C and pressures of 0.5, 1, 3, and 5 MPa. The ZnO-nanoparticle catalyst showed superior performance, achieving a maximum CO_2 conversion of

30.1% at 5 MPa and 300°C. The highest methanol yield, reaching 108 mg/g_{cat}·h, was attained at 280°C and 5 MPa. Throughout the experiments, carbon monoxide, methanol, ethanol, methyl formate, dimethyl ether, propanol, isobutyl, and isopropanol were detected.

Acknowledgements

This study was financially supported by the Russian Science Foundation, grant No. 20-79-10097.

Author Contributions

Artyom N.Markov: Conceptualization, Project administration, Writing – review and editing; Anna A. Golovacheva: Formal analysis, Investigation; Writing – original draft; , Alexander A. Kapinos: Investigation, Methodology; Egor S. Dokin: Investigation, Methodology; Pavel P. Grachev: Software; Anton N. Petukhov: Supervision; Artem Atlaskin: Software, Validation; , Vitaly A. Medov: Data curation, Validation; Sergey S. Suvorov: Data curation; Andrey V. Vorotyntsev: Supervision.

Conflict of Interest

The authors declare that there are no conflicts of interest.

References

Beck, A, Newton, MA, van de Water, LGA & van Bokhoven, JA 2024, 'The enigma of methanol synthesis by Cu/ZnO/Al_2O_3-based catalyst', *Chemical Reviews*, vol. 124, no. 8, pp. 4543–4678, https://doi.org/10.1021/acs.chemrev.3c00148

Bian, Z, Das, S, Wai, MH, Hongmanorom, P & Kawi, S 2017, 'A review on bimetallic nickel-based catalyst for CO_2 reforming of methane', *ChemPhysChem*, vol. 18, no. 22, pp. 3117-3134, https://doi.org/10.1002/CPHC.201700529

Busacca, CA, Fandrick, DR, Song, JJ & Senanayake, CH 2011, 'The growing impact of catalysis in the pharmaceutical industry', *Advanced Synthesis and Catalysis*, vol. 353, no. 11, pp. 1825-1864, https://doi.org/10.1002/adsc.201100488

Gao, P, Li, F, Zhao, N, Xiao, F, Wei, W, Zhong, L & Sun, Y 2013, 'Influence of modifier (Mn, La, Ce, Zr and Y) on the performance of Cu/Zn/Al catalyst via hydrotalcite-like precursors for CO_2 hydrogenation to methanol', *Applied Catalysis A: General*, vol. 468, pp. 442-452, https://doi.org/10.1016/j.apcata.2013.09.026

Gómez-Rodríguez, C, Fernández-González, D, García-Quiñonez, LV, Castillo-Rodríguez, GA, Aguilar-Martínez, JA & Verdeja, LF 2019, 'MgO refractory doped with ZrO2 nanoparticles: Influence of cold isostatic and uniaxial pressing and sintering temperature in the physical and chemical properties', *Metals*, vol. 9, no. 12, article 1297, https://doi.org/10.3390/met9121297

Guo, Y, Wen, M, Li, G & An, T 2021, 'Recent advances in VOC elimination by catalytic oxidation technology onto various nanoparticles catalyst: A critical review', *Applied Catalysis B: Environmental*, vol. 281, article 119447, https://doi.org/10.1016/j.apcatb.2020.119447

Hepburn, C, Adlen, E, Beddington, J, Carter, EA, Fuss, S, Mac Dowell, N, Minx, JC, Smith, P & Williams, CK 2019, 'The technological and economic prospects for CO2 utilization and removal', *Nature*, vol. 575, pp. 87–97, https://doi.org/10.1038/S41586-019-1681-6

Jangam, A, Hongmanorom, P, Hui Wai, M, Jeffry Poerjoto, A, Xi, S, Borgna, A & Kawi, S 2021, 'CO_2 hydrogenation to methanol over partially reduced Cu-SiO_2P catalyst: The crucial role of hydroxyls for methanol selectivity', *ACS Applied Energy Materials*, vol. 4, no. 11, pp. 12149-12162, https://doi.org/10.1021/acsaem.1c01734

Jiang, XY, Yang, WB, Song, H, Ma, QX, Gao, XH, Li, P & Zhao, TS 2023, 'Formic acid assisted synthesis of Cu-ZnO-Al_2O_3 catalyst and its performance in CO_2 hydrogenation to methanol', *Journal of Fuel Chemistry and Technology*, vol. 51, no. 1, pp. 120-128, https://doi.org/10.1016/S1872-5813(22)60041-0

Kalubowila, KDRN, Gunewardene, MS, Jayasingha, JLK, Dissanayake, D, Jayathilaka, C, Jayasundara, JMD, Gao, Y & Jayanetti, JKDS 2021, 'Reduction-induced synthesis of reduced graphene oxide-wrapped Cu_2O/Cu nanoparticles for photodegradation of methylene blue', *ACS Applied Nano Materials*, vol. 4, no. 3, pp. 2673-2681, https://doi.org/10.1021/acsanm.0c03320

Karunakaran, G, Sudha, KG, Ali, S & Cho, EB 2023, 'Biosynthesis of nanoparticles from various biological sources and its biomedical applications', *Molecules*, vol. 28, no. 11, article 4527, https://doi.org/10.3390/molecules28114527

Khan, I, Saeed, K & Khan, I 2019, 'Nanoparticles: Properties, applications and toxicities', *Arabian Journal of Chemistry*, vol. 12, no. 7, pp. 908–931, https://doi.org/10.1016/j.arabjc.2017.05.011

Khatami, M, Alijani, HQ, Nejad, MS & Varma, RS 2018, 'Core@shell nanoparticles: Greener synthesis using natural plant products', *Applied Sciences (Switzerland)*, vol. 8, no. 3, article 411, https://doi.org/10.3390/app8030411

Kong, XP, You, XM, Yuan, PH, Wu, YH, Wang, RH & Chen, JG 2023, 'Influence of dopants on the structure and catalytic features of the Cu/ZnO catalyst for dimethyl oxalate hydrogenation to ethylene glycol', *Journal of Fuel Chemistry and Technology*, vol. 51, no. 6, pp. 794-803, https://doi.org/10.1016/S1872-5813(22)60073-2

Kusrini, E, Harjanto, S & Yuwono, AH 2015, 'Applications of a green chemistry design, a clean environment, and bioenergy to promote the sustainability and added value of products', *International Journal of Technology*, vol. 6, no. 7, pp. 1065–1068, https://doi.org/10.14716/ijtech.v6i7.2787

Kusrini, E, Rafdi, AR, Usman, A, Wilson, LD, Degirmenci, V, Abdullah, MAA & Sofyan, N 2024, 'Performance comparison of heterogeneous catalyst based on natural Bangka kaolin for biodiesel production by acid and base activation processes', *International Journal of Technology*, vol. 15, no. 6, pp. 1994-2008, https://doi.org/ 10.14716/ijtech.v15i6.7023

Li, W, Wang, H, Jiang, X, Zhu, J, Liu, Z, Guo, X & Song, C 2018, 'A short review of recent advances in CO_2 hydrogenation to hydrocarbons over heterogeneous catalyst', *RSC Advances*, vol. 8, no. 14, pp. 7651-7669, https://doi.org/10.1039/C7RA13546G

Madani, H, Wibowo, A, Sasongko, D, Miyamoto, M, Uemiya, S & Budhi, YW 2024, 'Novel multiphase CO_2 photocatalysis system using N-TiO_2/CNCs and CO_2 nanobubble', *International Journal of Technology*, vol. 15, no. 2, pp. 432-441, https://doi.org/10.14716/ijtech.v15i2.6694

Markov, AN, Vorotyntsev, AV, Kapinos, AA, Petukhov, AN, Pryakhina, VI, Kazarina, OV, Atlaskin, AA, Otvagina, KV, Vorotyntsev, VM & Vorotyntsev, IV 2022, 'Direct synthesis of Al, Mg, Ni, and Ti nanoparticles by induction flow levitation technique', *ACS Sustainable Chemistry and Engineering*, vol. 10, no. 24, pp. 7929-7941, https://doi.org/10.1021/acssuschemeng.2c00940

Meng, A, Xing, J, Li, Z & Li, Q 2015, 'Cr-doped ZnO nanoparticles: Synthesis, characterization, adsorption property, and recyclability', *ACS Applied Materials and Interfaces*, vol. 7, no. 49, pp. 27449-27457, https://doi.org/10.1021/acsami.5b09366

Mulyatun, M, Prameswari, J, Istadi, I & Widayat, W 2022, 'Production of non-food feedstock based biodiesel using acid-base bifunctional heterogeneous catalyst: A review', *Fuel*, vol. 314, article 122749, https://doi.org/10.1016/j.fuel.2021.122749

Ou, Y, Zhang, T, Lv, L, Tang, W & Tang, S 2023, 'Investigation of Cu-ZnO/SiO_2 catalyst for CO_2 hydrogenation: Effect of SiO_2 support with different porous structure', *Colloids and Surfaces A: Physicochemical and Engineering Aspects*, vol. 676, article 132167, https://doi.org/10.1016/j.colsurfa.2023.132167

Pajor-Świerzy, A, Szczepanowicz, K, Kamyshny, A & Magdassi, S 2022, 'Metallic core-shell nanoparticles for conductive coatings and printing', *Advances in Colloid and Interface Science*, vol. 299, article 102578, https://doi.org/10.1016/j.cis.2021.102578

Qi, J & Hu, X 2020, 'The loss of ZnO as the support for metal catalyst by H_2 reduction', *Physical Chemistry Chemical Physics*, vol. 22, no. 7, pp. 3953-3958, https://doi.org/10.1039/C9CP06093F

Ren, J, Cao, JP, Zhao, XY & Liu, YL 2022, 'Recent progress and perspectives of catalyst design and downstream integration in biomass tar reforming', *Chemical Engineering Journal*, vol. 429, article 132316, https://doi.org/10.1016/j.cej.2021.132316

Ren, Y, Yang, Y & Wei, M 2023, 'Recent advances on heterogeneous non-noble metal catalyst toward selective hydrogenation reactions', *ACS Catalysis*, vol. 13, no. 13, pp. 8902-8924, https://doi.org/10.1021/acscatal.3c01442

Shawabkeh, RA, Faqir, NM, Rawajfeh, KM, Hussein, IA & Hamza, A 2022, 'Adsorption of CO_2 on Cu/SiO_2 nano-catalyst: Experimental and theoretical study', *Applied Surface Science*, vol. 586, article 152726, https://doi.org/10.1016/j.apsusc.2022.152726

Thao, NT, Nga, HTP, Vo, NQ & Nguyen, HDK 2017, 'Advanced oxidation of rhodamine B with hydrogen peroxide over Zn–Cr layered double hydroxide catalyst', *Journal of Science: Advanced Materials and Devices*, vol. 2, no. 3, pp. 317–325, https://doi.org/10.1016/j.jsamd.2017.07.005

Tuktin, B, Omarova, A, Saidilda, G, Nurzhanova, S, Tungatarova, S & Ongarbayev, Y 2024, 'Modified polymetallic zeolite-based catalyst for hydroprocessing diesel oil fraction and tetradecane', *International Journal of Technology*, vol. 15, no. 4, pp. 812-823, https://doi.org/10.14716/ijtech.v15i4.6746

Vorotyntsev, AV, Markov, AN, Kapinos, AA, Petukhov, AN, Atlaskin, AA, Golovacheva, AA, Vilkov, IV, Yunin, PA, Vorotyntsev, VM & Vorotyntsev, IV 2022, 'Direct synthesis of nanostructural and nanospherical silica using induction jet levitation: synthesis, design and catalytic application', *Materials Today Chemistry*, vol. 26, article 101004, https://doi.org/10.1016/j.mtchem.2022.101004

Vorotyntsev, AV, Markov, AN, Kapinos, AA, Petukhov, AN, Pryakhina, VI, Nyuchev, AV, Atlaskina, ME, Andronova, AA, Markova, EA & Vorotyntsev, VM 2020, 'Synthesis and comparative characterization of functionalized nanoporous silica obtained from tetrachloro- and tetraethoxysilane by a sol-gel method', *Phosphorus, Sulfur and Silicon and the Related Elements*, vol. 196, no. 2, pp. 176-188, https://doi.org/10.1080/10426507.2020.1825433

Wahyono, Y, Hadiyanto, Budihardjo, MA, Hariyono, Y & Baihaqi, RA 2022, 'Multifeedstock biodiesel production from a blend of five oils through transesterification with variation of moles ratio of oil: methanol', *International Journal of Technology*, vol. 13, no. 3, pp. 606–618, https://doi.org/10.14716/ijtech.v13i3.4804

Wang, M, Nakamura, K, Arifuku, M, Kiyoyanagi, N, Inoue, T & Kobayashi, Y 2022, 'Growth of single-walled carbon nanotubes from solid carbon nanoparticle seeds via cap formation engineering with a two-step growth process and water vapor supply', *ACS Omega*, vol. 7, no. 4, pp. 3639-3648, https://doi.org/10.1021/acsomega.1c06268

Wang, W, Wang, S, Ma, X & Gong, J 2011, 'Recent advances in catalytic hydrogenation of carbon dioxide', *Chemical Society Reviews*, vol. 40, no. 7, pp. 3703-3727, https://doi.org/10.1039/C1CS15008A

Whulanza, Y, Kusrini, E, Hermansyah, H, Sudibandriyo, M, Sahlan, M & Kartohardjono, S 2024, 'Catalyzing clean energy: The role of hydrogen and ammonia technology processes', *International Journal of Technology*, vol. 15, no. 4, pp. 803–811, https://doi.org/10.14716/ijtech.v15i4.7171

Xie, C, Niu, Z, Kim, D, Li, M & Yang, P 2020, 'Surface and interface control in nanoparticle catalysis', *Chemical Reviews*, vol. 120, no. 2, pp. 1184-1249, https://doi.org/10.1021/acs.chemrev.9b00220

Yang, H, Gao, P, Zhang, C, Zhong, L, Li, X, Wang, S, Wang, H, Wei, W & Sun, Y 2016, 'Core-shell structured Cu@m-SiO_2 and Cu/ZnO@m-SiO_2 catalyst for methanol synthesis from CO_2 hydrogenation', *Catalysis Communications*, vol. 84, pp. 56-60, https://doi.org/10.1016/j.catcom.2016.06.010

Yin, P, Hu, S, Qian, K, Wei, Z, Zhang, L-L, Lin, Y, Huang, W, Xiong, H, Li, W-X, Liang, H-W 2021, 'Quantification of critical particle distance for mitigating catalyst sintering', *Nature Communications*, vol. 12, no. 1, article 4865, https://doi.org/10.1038/s41467-021-25116-2

Ying, Z, Diao, J, Wang, S, Cai, X, Cai, Y, Liu, H & Wang, N 2021, 'Thermal stability, ripening dynamics and coalescing microstructures of reduced graphene oxide-based platinum nanocatalyst: An in-situ TEM study', *Diamond and Related Materials*, vol. 120, article 108690, https://doi.org/10.1016/j.diamond.2021.108690

Zhao, D, Wan, Y & Zhou, W 2013, *Ordered mesoporous materials*, John Wiley & Sons, https://doi.org/10.1002/9783527647866

Zhao, F, Liu, Y, Lu, N, Xu, T, Zhu, G & Wang, K 2021, 'A review on upgrading and viscosity reduction of heavy oil and bitumen by underground catalytic cracking', *Energy Reports*, vol. 7, pp. 4249-4272, https://doi.org/10.1016/j.egyr.2021.06.094

Zhao, G, Huang, X, Wang, X & Wang, X 2017, 'Progress in catalyst exploration for heterogeneous CO_2 reduction and utilization: A critical review', *Journal of Materials Chemistry A*, vol. 5, no. 41, pp. 21625-21649, https://doi.org/10.1039/C7TA07290B